Editors' Suggestion

On-Chip Coherent Transduction between Magnons and Acoustic Phonons in Cavity Magnomechanics

D. Hatanaka,* M. Asano, H. Okamoto, Y. Kunihashi, H. Sanada, and H. Yamaguchi
NTT Basic Research Laboratories, NTT Corporation, Atsugi-shi, Kanagawa 243-0198, Japan

(Received 2 November 2021; revised 16 January 2022; accepted 9 February 2022; published 8 March 2022)

Coherent control of collective spin excitations (magnons) with acoustic phonons is a key technology for future hybrid spintronics devices. Surface acoustic waves (SAWs), owing to their high frequency, short wavelength, and low radiation loss, could provide an appropriate platform for integrating the devices on a chip. However, the tiny coupling efficiency in previous experiments using traveling SAWs limits the availability of this prospect. We report a planar cavity magnomechanical system, where standing acoustic waves (i.e., a SAW cavity) enhance the spatial and spectral power density to implement magnified magnon-phonon coupling. Excitation of spin-wave resonance involves significant acoustic power absorption approaching 90%, whereas the collective spin motion exerts hybridization force on the cavity dynamics, leading to coupling cooperativity exceeding unity at room temperature in such a chip-scale device. The cavity magnomechanical system paves the way to the coherent acoustic control of magnons and the development of alternative spin-acoustic technologies for classical and quantum applications.

DOI: 10.1103/PhysRevApplied.17.034024

I. INTRODUCTION

Acoustic phonons allow interconnections between different physical systems and have attracted attention, especially in the fields of cavity optomechanics [1–6] and circuit quantum acoustodynamics [7–15]. In contrast to electromagnetic microwaves, acoustic waves have a short micrometer-scale wavelength, namely a slow propagation speed, at gigahertz frequencies and no radiation loss into free space. Owing to these unique properties, hybrid acoustic devices are spatially compact and enable coherent signal manipulation. Thus, an understanding of their interaction with phonons and an ability to exploit it can import these advantageous features of phonons into other physical systems and extend the functionality of hybrid systems.

The magnon-phonon interaction via magnetoelastic coupling has recently stimulated interdisciplinary research in the fields of mechanics and spintronics, where gigahertz spin oscillations parametrically interact with megahertz acoustic vibrations via electromagnetic cavity resonances [16,17], and resonantly couple to frequency matched vibrations [18–29]. In addition to the benefits mentioned above, hybridization with a phonon enables a magnon to acquire the low-loss property of the phonon and form magnetoelastic waves (magnon polaron), resulting in improved coherence [30,31]. On the other hand, the phonon gains the magnetic susceptibility of the magnon, carrying spin angular momentum and demonstrating nonreciprocal propagation [20,24–26,29]. To explore the potential application, a SAW device has been employed as an alternative platform and has succeeded in acoustically driving spin wave oscillations [19,20,22–29,32]. This chip-scale magnomechanical structure can utilize the short acoustic wavelength for a planar integrated circuit and, unlike ferromagnetic sphere [17] and bulk-acoustic-wave resonators [18,21], is compatible with current SAW-based sensing and communications device technologies. Moreover, this allows for advanced acoustic manipulations by introducing developed phononics technology such as phononic crystal. In spite of the potential, previous experiments have focused on traveling acoustic waves, whose weak mutual interaction makes it difficult to fully explore the features of resonant magnon-phonon coupling (i.e., coherent magnon excitation by acoustic means and the hybridization effect on acoustic resonance).

Here, we demonstrate on-chip cavity-enhanced transduction of spin-wave oscillations via magnetostriction at room temperature. We observe enhancement of the acoustic excitation efficiency of magnons and the hybrid effect on the SAWs with increasing acoustic quality factor and reveal cooperativity exceeding unity by comparing measurement results with a theoretical magnomechanical model. This will lead to the generation of magnon polarons on a chip and facilitate the application of the magnomechanical physics and technology to radio-frequency information processing in classical and quantum regimes.

*daiki.hatanaka.hz@hco.ntt.co.jp

II. RESULTS

Our cavity magnomechanical system was constructed on a $LiNbO_3$ substrate as shown in Figs. 1(a) and 1(b). It is piezoelectrically excited through an interdigital transducer (IDT), and the vibrations are resonantly enhanced by Bragg reflectors, forming a cavity [33,34]. The magnetization of a nickel (Ni) film is driven by the acoustic waves via a magnetostriction, generating collective spin resonance. This excitation dynamics is investigated by electrically measuring SAW transmission (S_{21}) at room temperature and in a vacuum. The details on the device and measurement configuration are discussed in Appendix A.

First, the spectral response of the acoustic cavity is investigated by exciting SAWs through an IDT and measuring them from another IDT as shown in Fig. 1(c). Multiple peaks appear in the frequency range from 0.963 to 1.007 GHz, where they are equally separated by $\Delta f = 3.0$ MHz. The SAW velocity of $LiNbO_3$ is estimated to be $v_{\mathrm{SAW}} = \omega_a/k = 3900$ m/s from measured resonance angular frequency ω_a and wave number k, which is consistent with a previous report [35]. Then, the cavity length is $L_c = v_{\mathrm{SAW}}/(2\Delta f) = 650\ \mu$m, which almost corresponds to $d_1 + 2d_2$, indicating that the observed peaks are Fabry-Perot (FP) resonances by two Bragg reflectors. Figure 1(d) shows the quality factor of each resonance (Q_a) as a function of frequency, where it increases to 5000 in the frequency range between 0.970 and 0.975 GHz. The enhancement of Q_a results from the bandgap formed in the reflectors, which can be predicted by the finite-element method (see Appendix B). Thus, incorporating the acoustic reflectors into the system suppresses energy dissipation and provides a high-quality acoustic cavity.

Acoustic excitation of the spin-wave resonance is then demonstrated by measuring acoustic transmission (S_{21}) at 0.9748 GHz in the FP resonance labeled P1 [see Fig. 1(c)] while sweeping both the strength [$\mu_0 H_{\mathrm{ex}}$] and directed angle [ϕ_h defined in Fig. 2(a)] of the external in-plane magnetic field. Figure 2(b) shows the transmission magnitude $|S_{21}|^2$ normalized by that under the off-spin-wave resonance condition at $\mu_0 H_{\mathrm{ex}}^{\mathrm{ref}} = 30$ mT. The angle dependence displays the well-known butterfly shape, which has been reported in SAW-based magnetostrictive systems [19,23,28]. It should be noted that the SAW amplitude is minimized at $\mu_0 H_{\mathrm{ex}} = 2$ mT and $\phi_h = 45^\circ$ and the absorption level is much larger than that at similar frequencies

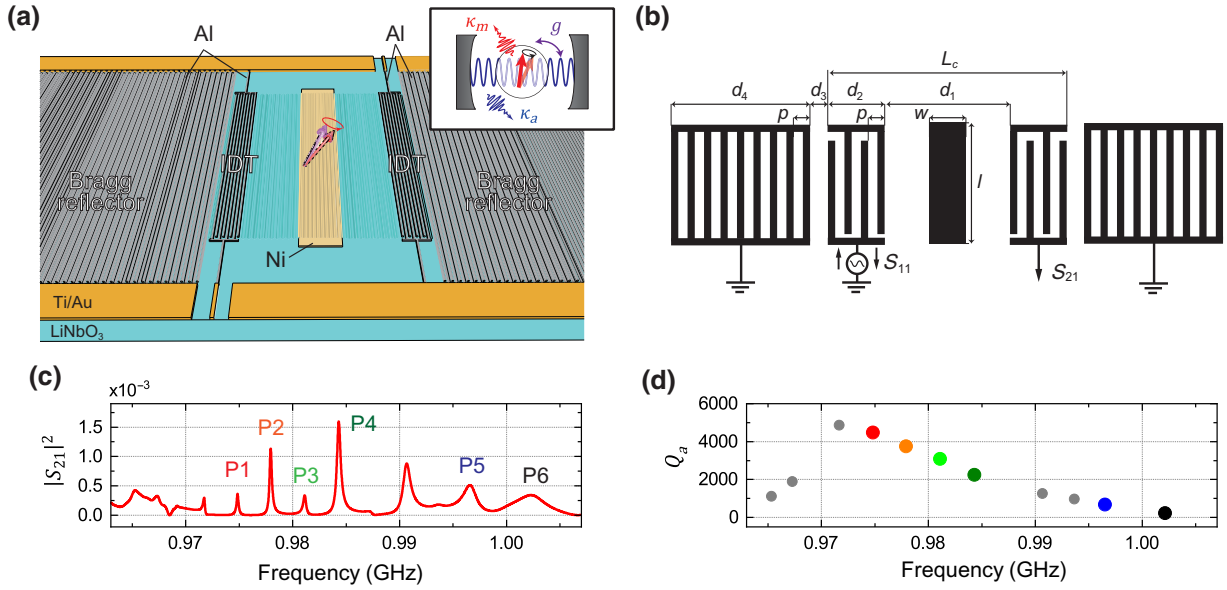

FIG. 1. Schematic of cavity magnomechanical system based on a SAW resonator on a $LiNbO_3$ substrate. Acoustic Bragg reflectors composed of a one-dimensional periodic structure made of aluminum thin films are formed outside of both interdigital transducers (IDTs), which enables acoustic waves to be confined via the bandgap effect. A rectangular Ni film is deposited between the IDTs. A static magnetic field ($\mu_0 H_{\mathrm{ex}}$) is applied in the plane of the film and aligns the magnetic moments. The inset is a schematic diagram of a cavity magnomechanical model where a magnonic cavity (i.e., spin-wave resonance) with angular frequency ω_m and damping κ_m interacts with an acoustic cavity with damping κ_a via coupling g. (b) The device geometry, where $d_1 = 557\ \mu$m, $d_2 = 77\ \mu$m, $d_3 = 2.9\ \mu$m, $d_4 = 1137\ \mu$m, $p = 2.0\ \mu$m, $w = 120\ \mu$m, and $l = 750\ \mu$m. (c),(d) Frequency dependence of the SAW transmission ($|S_{21}|^2$) and quality factor (Q_a), respectively. Fabry-Perot resonances denoted by solid color circles in (d) are labeled P1 (red), P2 (orange), P3 (light green), P4 (green), P5 (blue), and P6 (black).

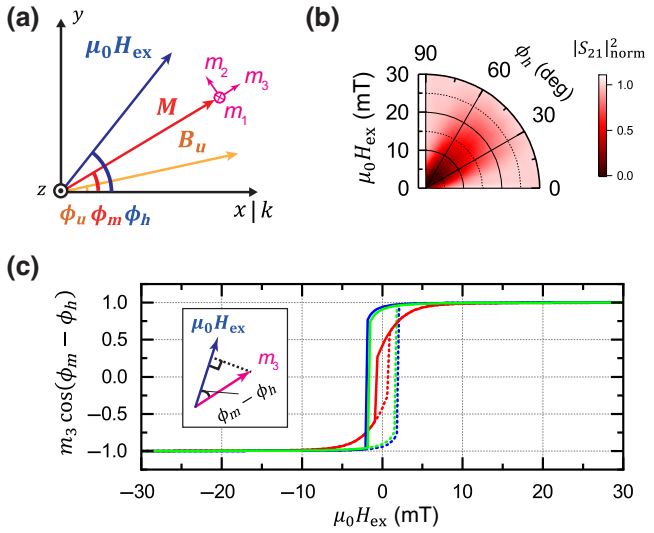

FIG. 2. (a) Coordinates of external magnetic field ($\mu_0\mathbf{H}_{ex}$), magnetization (**M**), and uniaxial anisotropic field ($\mathbf{B}_u$) with angle ϕ_h, ϕ_m, and ϕ_u with respect to the x axis, which is parallel to the SAW wave vector (k). Alternative coordinate system with $\mathbf{m} = (m_1, m_2, m_3)$, where m_3 is aligned to the equilibrium magnetization orientation. (b) Normalized acoustic transmission $|S_{21}|^2_{norm} \equiv |S_{21}(\omega)|^2/|S_{21}(\omega)|^2_{ref}$ in P1 resonance as function of external field $\mu_0 H_{ex}$ measured at frequency $\omega/2\pi = 0.9748$ GHz as the field angle is changed from $\phi_h = 0°$ to 90°. Here, $|S_{21}(\omega)|_{ref}$ is the value at reference field $\mu_0 H^{ref}_{ex} = 30$ mT, which is chosen because of the off-resonance condition of the magnon-phonon coupling. Acoustic power suppression due to spin-wave resonance excitation is observed around $\mu_0 H_{ex} = 2.1$ mT at $\phi_h = 45°$. (c) Static magnetization dynamics as function of field $\mu_0 H_{ex}$ at $\phi_h = 90°$ (red), 45° (blue), and 0° (green) calculated with the Stoner-Wohlfarth model, where the projection of m to the field direction $[\cos(\phi_m - \phi_h)]$ as denoted in the left inset, is plotted on the y axis. The results obtained during backward and forward sweeps are shown as solid and dotted lines, respectively.

in previous reports. This is ascribed to the resonance frequency of the magnetic precession (ω_m) approaching ω_a so that efficient spin-wave driving using the acoustic vibrations becomes possible in the cavity magnomechanical system (see also the simulated results in Appendix C).

Before showing the detailed field response, we theoretically confirm the equilibrium magnetization dynamics of the Ni film for three specific field directions ($\phi_h = 90°$, 45°, and 0°). The magnetization dynamics of the Ni film is mainly governed by the external magnetic field ($\mu_0\mathbf{H}_{ex}$), in-plane uniaxial anisotropy ($\mathbf{B}_u$), and out-of-plane shape anisotropy ($\mathbf{B}_d$). Figure 2(a) displays the relationship among these vectors in an xy coordinate system, where ϕ_h, ϕ_m, and ϕ_u are the angle of $\mu_0\mathbf{H}_{ex}$, magnetization vector **M**, and the easy axis of in-plane uniaxial anisotropy, respectively, from the SAW propagation direction (x axis). The magnetic free energy density normalized to the saturation magnetization (M_s) is given by

$$G = -\mu_0\mathbf{H}_{ex}\cdot\mathbf{m} - B_u(\mathbf{m}\cdot\mathbf{u})^2 + B_d m_z^2, \tag{1}$$

where **M** and **u** are the unit vectors of magnetization (**M**) and easy axis of in-plane uniaxial anisotropy. The equilibrium position of the magnetization is determined so as to minimize G.

The magnetization components projected to the field at $\phi_h = 90°$, 45°, and 0° are simulated by assuming $\phi_u = 25°$ as shown in Fig. 2(c). When the field is strong enough (e.g., $\mu_0 H_{ex} = 30$ mT), the magnetization is perfectly aligned with it. As the field decreases in the backward sweep, the magnetization is oriented toward the uniaxial anisotropy axis from the field direction. At $\phi_h = 0°$ (45°), the rotation starts from $\phi_m = 0°$ (45°) around 2 mT, and ϕ_m is aligned with $\phi_u = 25°$ at 0 mT. The rotation continues to $\phi_m = 45°$ (0°), and then it is inverted and finally reoriented to the negative field, that is, $\phi_m = 180°$ (225°). On the other hand, this rotation gradually starts from 10 mT at $\phi_h = 90°$, in which the magnetization angle gradually changes from $\phi_m = 90°$ to 10°, passing through $\phi_u = 25°$, and inversion occurs at −0.6 mT. Even after the inversion, the rotation continues from 215° to the field direction, 270°. This simulation reveals that the equilibrium magnetization is not always parallel to the field and its orientation is governed by the relationship between the external and anisotropic fields. In analyzing the magnetomechanical coupling effect, the effect of this magnetization rotation should be taken into account. This equilibrium magnetization dynamics is described in more detail in Appendix D.

We then measured the field response of S_{21} for these three field directions as shown in Fig. 3 . We also compared the response of six different FP resonances, P1–P6, to confirm the effect of the quality factor (i.e., the cavity confinement). For all three magnetic field directions, the backward field sweep from $\mu_0 H_{ex} = 30$ mT reduces the acoustic magnitude because the efficiency of the magnetostrictive spin driving is enhanced. It is remarkable that the acoustic absorption power is amplified as Q_a increases and approaches 80%–90% at these angle configurations, which is much larger than in previous systems (less than 10%) [19,28]. Obviously, the enhancement of the acoustic absorption is a consequence of the cavity effect of our magnomechanical system (see Appendices E and F for further discussion of the results).

The different field responses observed for the three field directions are explained by the magnetization dynamics already discussed [Fig. 2(c)]. We need to take into account two contributions. One is the variation of magnetostriction coupling constant J defined by

$$J = kb_{ma}\sin 2\phi_m V_{ma}. \tag{2}$$

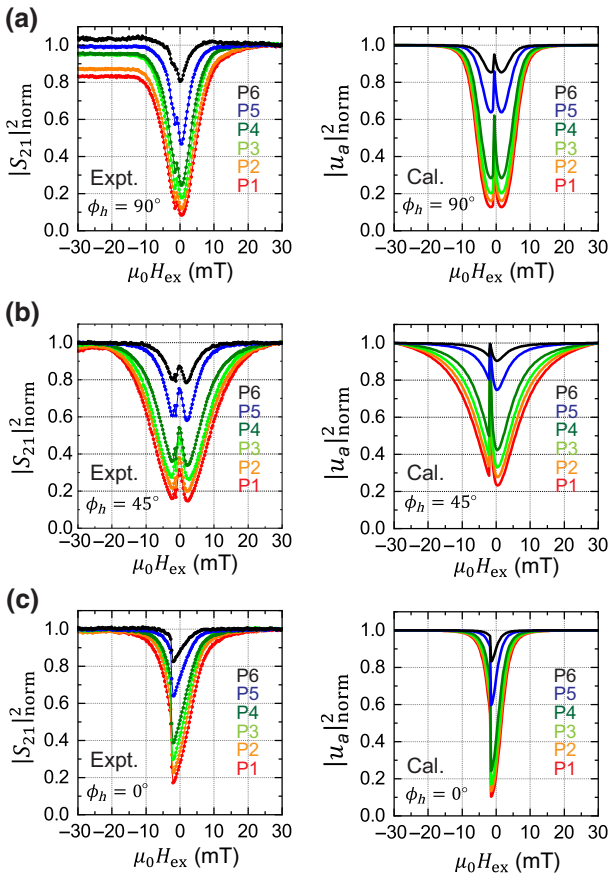

FIG. 3. (a),(b),(c) Field $\mu_0 H_{\rm ex}$ response of the acoustic transmission measured in P1–P6 resonances with various Q_a in $\phi_h = 90°$ (a), 45° (b) and 0° (c), obtained by experiment (left) and calculation (right). The results on the Fabry-Perot resonance with $Q_a = 4500$ (P1, red), 3800 (P2, orange), 3200 (P3, light green), 2300 (P4, green), 700 (P5, blue), and 200 (P6, black) are plotted, in colors corresponding to those in Fig. 1(d). The normalized acoustic vibration is calculated by $|u_a|^2_{\rm norm} = |u_a|^2/|u_a|^2_{\rm ref}$, where $|u_a|_{\rm ref}$ is the value at $\mu_0 H_{\rm ex} = 30$ mT. Dual dips at $\phi_h = 90°$ and 45° and a single dip at $\phi_h = 0°$ are generated as a consequence of the acoustic excitation of spin-wave resonance.

Here, $b_{\rm ma}$ is the magnetoelastic coupling constant, and $V_{\rm ma}$ is the effective mode overlap of the magnetostriction. Obviously, the absolute value of J changes with magnetization rotation and becomes maximum at $\phi_m = 45°(2n+1)$, $n = 0, 1, 2, \ldots$. The other contribution is the spin resonance effect, where the maximum efficiency is obtained when magnonic resonance frequency ω_m matches the acoustic drive frequency ω. The displacement amplitude (u_a) of acoustic waves is given by

$$u_a(\omega) = \frac{F_d \rho_a^{-1}}{-(\omega^2 - \omega_a^2) - i\omega\kappa_a - J^2\chi_m(\omega)}, \qquad (3)$$

where $\chi_m(\omega) = 2M_s\gamma\eta\omega_m/\{\rho_a V_a V_m(1+\alpha^2)(-\omega^2 + \omega_m^2 + \frac{\kappa_m^2}{4} - i\kappa_m\omega)\}$ is the magnonic susceptibility. In the expressions, F_d, ρ_a, and γ are the driving force density, mass density, and gyromagnetic ratio, and V_a (V_m) and η denote the effective mode volume of the acoustic (magnonic) system and the magnetoelastic coefficient, respectively. The resonance angular frequency and damping rate of the acoustic (magnonic) system are denoted by ω_a and κ_a (ω_m and κ_m), respectively [see Appendix G for the detailed derivation of Eq. (3) and the parameters]. The field response of SAW absorption efficiency is determined by taking into account the following two contributions: the change in J caused by the field-induced magnetization rotation and the coupling enhancement by the spin resonance condition.

From Eqs. (2) and (3), the dynamics of the cavity magnomechanical system illustrated in the inset of Fig. 1(a) was simulated using the parameters as described in Appendix H. The right panels of Fig. 3 show the calculation results, where the normalized amplitude is plotted on the vertical axis. The calculation well reproduces the experimental results on the field and quality-factor dependencies for all three field directions even though they show different magnetization dynamics. This analysis indicates that high magnon-phonon coupling is obtained by applying the spin resonance condition while maintaining $\phi_m \sim 45°$ to obtain large magnetostriction effects.

The strong driving of the ferromagnetic spin-wave oscillations enables modulation of the acoustic dynamics via hybridization. The spectral response in P1 resonance is measured with a backward field sweep at $\phi_h = 90°$, 45°, and 0° as shown in the left panel of Figs. 4(a), 4(c), and 4(e), and the experimental quality factor Q'_a and resonance frequency $\omega'_a/(2\pi)$ acquired from the measured spectrum are plotted in Figs. 4(b), 4(d), and 4(f), respectively. At $\phi_h = 45°$, ω'_a and Q'_a are modulated with decreasing field and changes in polarity at $\mu_0 H_{\rm ex} = \pm 2.1$ mT. Similar field dependencies are also observed at $\phi_h = 90°$, but the width of the dips becomes narrow compared to that at $\phi_h = 45°$. The spin-wave oscillation is generated only in the magnetization rotation regime $|\mu_0 H_{\rm ex}| < 10$ mT in $\phi_h = 90°$, allowing the magnetostriction to be activated only by those fields ($J \neq 0$), and then J becomes a maximum when $\phi_m = 45°$ and 225° at the fields of the dips. On the other hand, this nonzero J is kept in almost the entire range between ±30 mT at $\phi_h = 45°$ because initially $\phi_m = \phi_h$. Hence, the available field for the hybridization is wider than in Fig. 4(b). Moreover, a different feature of the field response is observed at $\phi_h = 0°$ in Fig. 4(f), where a single dip appears at −1 mT. This is because $\phi_m = 45°$ only around the field. Since these experimental behaviors are reproduced by the theoretical model, the variation in ω'_a and Q'_a results from the dynamic hybridization of the spin-wave excitation, which more than doubles the acoustic damping rate.

The cavity effect on the magnetostrictive coupling is quantitatively investigated as a function of the acoustic

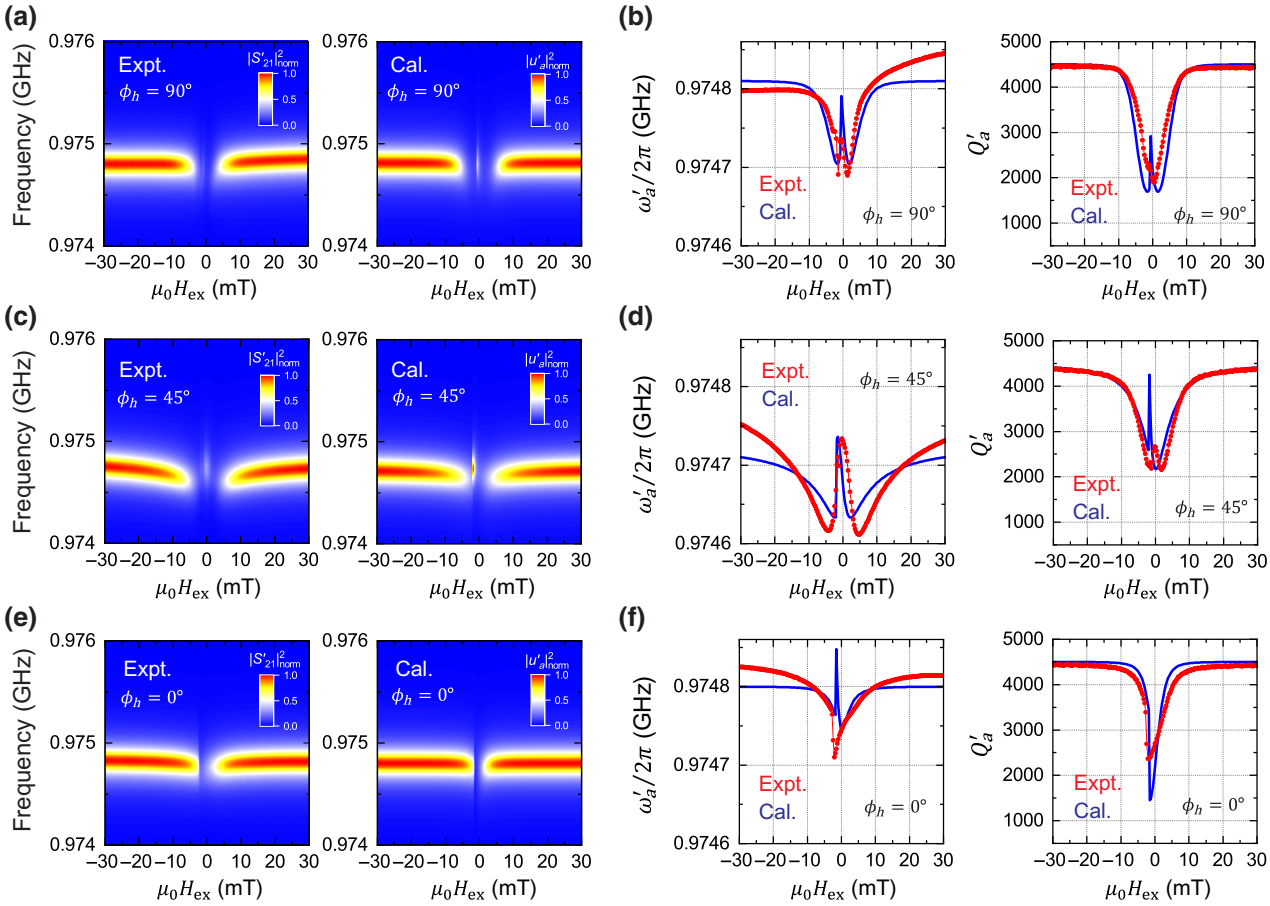

FIG. 4. (a),(c),(e) Left: Spectral responses of the acoustic resonance P1 at $\phi_h = 90°$, 45°, and 0°, respectively, as the field was swept from $\mu_0 H_{ex} = 30$ mT to -30 mT. The normalized magnitude $|S'_{21}|^2_{norm}$ is obtained from the value divided by that at $\mu_0 H^{ref}_{ex} = 30$ mT and at each acoustic resonance frequency. Right: Simulated spectral response of the acoustic magnitude $|u'_a|^2_{norm}$ at the corresponding ϕ_h. The resonance frequency used in the calculation was set to $\omega_a/2\pi = 0.974\,81$, $0.974\,73$, and $0.974\,80$ GHz, respectively. The different resonance frequency between $\phi_h = 90°$, 45°, and 0° might be caused by the effect of a static stress induced by the magnetostriction which is variant with changing field direction. The theoretical estimation is beyond the scope of this research. (b),(d),(f) Resonance frequency $\omega'_a/2\pi$ (left) and acoustic quality factor Q'_a (right) as a function of field $\mu_0 H_{ex}$ at $\phi_h = 90°$, 45°, and 0°, respectively. The experimental values obtained by fitting a Lorentzian curve to the measured spectra in (a)–(c) are shown by red solid circles. The calculation data obtained from Eqs. (2) and (3) described in Appendix G is shown by the blue solid line.

damping. To do so, we use cooperativity parameter C, the ratio of coherent magnon-phonon coupling rate (g) to κ_a and κ_m, which expresses the efficiency of coherent energy transfer between different physical systems and is commonly used in cavity optomechanics and circuit quantum acoustodynamics . In our cavity magnomechanical system,

$$C = \frac{\kappa'_a}{\kappa_a} - 1 = \frac{4g^2}{\kappa_m \kappa_a}, \tag{4}$$

where magnon-phonon coupling g is

$$g = J\sqrt{\frac{M_s \gamma \eta}{2V_a V_m \rho_a (\omega_a + \frac{\kappa_m^2}{16\omega_a})(1+\alpha^2)}}, \tag{5}$$

with total damping rate κ'_a. To obtain Eq. (4), we adopt the approximation that variation in ω'_a is negligibly smaller than that in κ'_a. The expression for g including η is derived from Eq. (3) only when the condition $\omega = \omega_a = \omega_m$ is satisfied (the detailed explanation can be found in Appendix G). Note that our system at $\phi_h = 90°$ can simultaneously fulfill the resonance coupling condition $\omega_m \approx \omega_a$ and the maximum magnetostriction $\phi_m \approx 45°$ in $\mu_0 H_{ex} = 0.6 \sim 1.8$ mT (see Appendix I). By extracting κ'_a from P1–P6 resonances at the field angle, C is plotted as a function of κ_a^{-1} as shown in Fig. 5. The C calculated from Eqs. (4) and (5) is also shown by a solid line. The experimental C increases with increasing κ_a^{-1}, namely Q_a, which is consistent with the calculation result. Finite deviation of the experimental results from the calculation ones might be caused by the difference in acoustic mode profiles in the

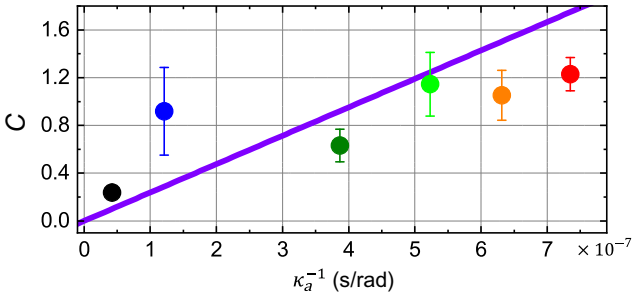

FIG. 5. Inverse of acoustic damping κ_a^{-1} dependence of cooperativity C, experimentally obtained by measuring the change in total acoustic damping κ_a' between $\mu_0 H_{\rm ex}^{\rm res} = 0.6$ mT and 1.8 mT at $\phi_h = 90^\circ$, as denoted by solid circles in colors corresponding to those of P1–P6 resonances [see Fig. 1(d)]. The theoretical prediction of C obtained from the Eqs. (4) and (5) is plotted by a purple solid line.

different FP resonances. Finally, the cooperativity reaches $C = 1.2 \pm 0.1$ in P1 resonance with $Q_a = 4500$, thus indicating coherent transduction between spin and acoustic waves. The coupling rate in our system is estimated to be $g = 2\pi(9.9 \pm 0.2)$ MHz, which is larger than the intrinsic acoustic damping but smaller than the magnetic one ($\kappa_m > g > \kappa_a$). In this way, the experimental coherent coupling with $C > 1$ and the evaluation of g are demonstrated in a piezoelectric SAW cavity with a Ni thin film. Such a ferromagnetic metal will be useful because it is deposited on various types of substrate and the magnetic property can be tailored by changing the structure with a standard microfabrication technology, in contrast to a ferromagnetic insulator such as yttrium-iron-garnet. Employing a low-magnetic damping metal such as Fe_3Si ($\alpha \sim 10^{-4}$) would be a valid way to further increase the effective interaction and achieve a strong coupling condition ($g > \kappa_a, \kappa_m$) [20].

III. CONCLUSION

We demonstrated on-chip coherent transduction between magnons and phonons in a SAW-based cavity magnomechanical system. Utilizing this platform, we have an opportunity to further improve functionality. For instance, combining it with spintronics technology, where ferromagnetic dynamics can be engineered by advanced microfabrication, will enable us to design the magnetoelastic effect, which will lead to robust and versatile spin excitation schemes unrestricted by the field configuration. The integration of a wavelength-scale phononic crystal structure in the system will be useful for enhancing the ability to spatially control acoustic waves [7,36], allowing the development of large-scale magnomechanical circuits. The phononic crystal platform can be excited by electrical means such as the piezoelectric effect, so it is compatible with sophisticated electronics technology. Thus, our cavity magnomechanical system will open up the possibility of controlling acoustic phonons with magnons and vice versa, which holds promise for establishing alternative magnon-phonon technologies for classical and quantum signal processing applications.

ACKNOWLEDGMENTS

The authors thank H. Murofushi and S. Sasaki for support with the nickel deposition and sample preparation. D.H. fabricated the device and performed the measurements and the data analysis. M.A. made the theoretical model, and D.H., M.A., and H.Y. conducted the simulations with support from H.O. Finally, D.H., H.Y., and M.A. wrote the manuscript. All authors discussed the results in the course of preparation of the paper.

APPENDIX A: FABRICATION AND MEASUREMENT

The device was fabricated on a commercially available 128°-*Y* $LiNbO_3$ substrate (Black-LN, Yamaju Ceramics Co., Ltd.). A rectangular Ni thin film with a thickness of $d = 50$ nm was formed. Nickel was chosen because it has the highest magnetostrictive constant among common ferromagnets such as cobalt, permalloy, and iron. In the simulation, we considered out-of-plane shape anisotropy (B_d) and in-plane uniaxial anisotropy (B_u) in the ferromagnet. The former is caused by the thin-film structure, and the latter can accidentally occur during the film growth on the substrate or could be caused by the rectangular shape of the film. To sandwich it, two IDT electrodes with a thickness of 50 nm were introduced. They have 19 finger pairs with a pitch of $2p = 4.0$ μm, and were used to excite and detect SAW transmission piezoelectrically. Acoustic Bragg reflectors were built to confine the acoustic waves. They consisted of 568-periodicity strip lines with a pitch of $p = 2.0$ μm and were connected to electrical ground. Acoustic trapping in this cavity is a result of constructive interference between incident waves and reflected waves from the periodic metallic strip lines. These Bragg reflectors and IDTs are made of aluminum (Al) because its low mass density among metals allows gentle confinement of SAWs due to the relatively small acoustic reflectivity and suppresses coupling of reflected waves to bulk acoustic modes.

Resonant SAWs were measured from one IDT electrode in S_{21} with a network analyzer (E5080A, Keysight) by injecting microwave signals with -20 dBm into the other one. Spurious electromagnetic waves due to crosstalk between the IDTs were filtered out by a time-gating technique. Simultaneously, a static magnetic field was applied in the plane of the Ni thin film from an electromagnetic coil, and the field was swept backward, from $\mu_0 H_{\rm ex} = 30$ mT to 0 mT or -30 mT, in the experiments in Figs. 2, 3, and 4. All the measurements in this study were performed at room temperature and in moderate vacuum ($\sim 10^1$ Pa).

APPENDIX B: SAW-BASED ACOUSTIC CAVITY

The acoustic dynamics of the SAW resonator is investigated by the finite-element method. When the wavelength of traveling waves is satisfied by the Bragg condition $p = n\lambda_{\mathrm{SAW}}/2$ ($n = 1, 2, 3, \ldots$), reflected waves at metallic striplines interfere with incident waves. As shown in Fig. 6(a), the resultant waves form two different standing-wave modes, which have the same wavelength but different acoustic energy due to the different modal shape with respect to the stripline position. Therefore, a frequency gap, namely a bandgap, emerges, thus preventing the waves from propagating through the reflectors.

Thanks to the presence of the bandgap, SAWs are confined and then resonantly vibrate in an acoustic cavity formed by the Bragg reflectors. To investigate the cavity dynamics, we simulate acoustic resonance modes. In the model, perfectly matched layers are introduced at the bottom and sides of the structure to prevent the generation of unwanted reflections. Figure 6(b) shows the frequency dependence of the quality factor (Q) of calculated resonance modes between 0.870 and 0.900 GHz. The results indicate that Q is dramatically enhanced within the bandgap (highlighted in yellow). This is a consequence of suppression of leaky modes due to the cavity confinement. The simulated Qs are larger than the experimental ones because our simulation does not take other possible damping factors into account, such as thermoelastic damping, piezoelectricity-induced ohmic loss, and two-level system damping. The thermoelastic damping can be a dominant dissipation source at room temperature in such ultrahigh-frequency phononic devices [36,37]. Figure 6(c) reveals the modal shapes of two resonance modes, A and B, appearing in the bandgap [see in Fig. 6(b)]. Indeed, the bandgap confinement realizes resonance vibrations with high Q. The discrepancy between the resonance frequencies with the experimental ones could be caused by slight differences in elastic properties such as SAW velocity.

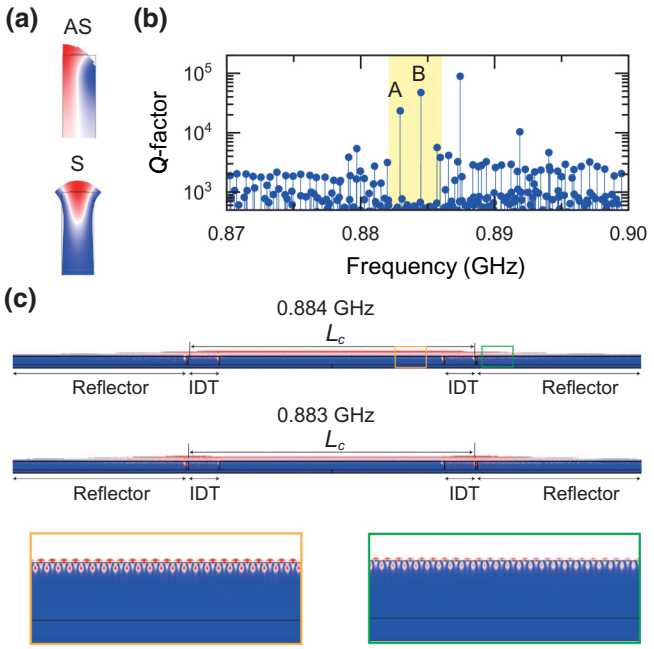

FIG. 6. (a) Simulated displacement of trapped modes in the Bragg reflector at the Brillouin zone edge. The S mode has an antinode displacement at the location of an Al metallic line, whereas the AS mode does not. This induces a frequency difference between these modes in spite of their having the same wave number. A unit structure of the reflector is shown by black solid lines. (b) Frequency dependence of a calculated Q-factor in a SAW resonator. Q is enhanced within the bandgap as highlighted in yellow. Two modes, labeled A and B, are cavity modes whose modal shapes are shown in (c). Modes showing high-Q outside the bandgap are not cavity modes; they are accidentally formed at the structure edges. (c) Displacement modal shapes of A and B at 0.883 and 0.884 GHz respectively, where SAWs are gently confined by the two Bragg reflectors with the cavity length L_c [see Fig. 1(b)]. The bottom insets show the zoom-in mode profile of SAW displacements in the cavity (left) and Bragg reflector (right).

APPENDIX C: SIMULATION OF THE FIELD-ANGLE RESPONSE OF ACOUSTICALLY DRIVEN SPIN-WAVE RESONANCE

Figure 7 shows the field dependence of the normalized acoustic absorption $|u_a|^2_{\mathrm{norm}}$, calculated at various field angles ϕ_h ranging from 0° to 90°. Significant absorption occurs in a broad range between $\phi_h = 30°$ and 75°. Slightly different from the experimental result in Fig. 2(b), the simulated butterfly shape shifts toward higher ϕ_h. This discrepancy might be due to the contribution from the static magnetostriction in the experiment. Applying an external field to the Ni film induces static stress in it via the magnetostriction, allowing the resonance frequency to be modified. This effect was not considered in the calculation.

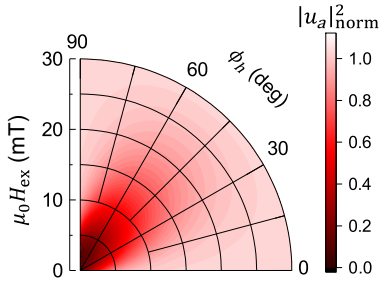

FIG. 7. Calculated absorption in the normalized SAW transmission $|u_a|^2_{\mathrm{norm}}$ due to the acoustic excitation of spin-wave precession in the range between $\phi_h = 0°$ and 90°. In the simulation, acoustic frequency $\omega/2\pi = \omega_a/2\pi = 0.9748$ GHz is used to solve Eq. (3) in the main text.

APPENDIX D: MAGNETIZATION ROTATION WHILE SWEEPING AN EXTERNAL FIELD

Due to the in-plane anisotropy of the Ni film, the magnetic moments m is deviated from the external field direction $\mu_0 H_{\rm ex}$ and undergoes rotation and inversion while the field is swept. Figures 8 shows the magnetization angle ϕ_m as function of the field in backward sweep ($\mu_0 H_{\rm ex} = 30$ mT to -30 mT) at $\phi_h = 90°$, $45°$, and $0°$, respectively. The right insets illustrate the magnetization direction m (red arrow) with respect to the field $\mu_0 H_{\rm ex}$ (blue arrow) and the in-plane anisotropic axis B_u (yellow solid line). Number labels ①, ②, ③, and ④ in the left figures indicate the resultant magnetization configuration at the fields. When the field is strong enough, the magnetization is parallel to it because the magnetic free energy G becomes minimized (①). As the field is decreased, however, it starts rotating to the anisotropy field and then is aligned at $\mu_0 H_{\rm ex} = 0$ mT (②). As the field in the negative field regime is further swept and reaches $\mu_0 H_{\rm ex} = -0.6$ mT ($\phi_h = 90°$) and -1.5 mT ($\phi_h = 45°$ and $0°$), the magnetization is instantaneously inverted (③) and, finally, is again aligned to the field direction (④). Clearly, the magnetization is not always aligned to the field, especially in the low-field range, and the magnetization angle ϕ_m can change between the field ϕ_h and the anisotropy field ϕ_u, thus resulting in the modification of the magnetostriction.

APPENDIX E: ENHANCED ACOUSTIC ABSORPTION DUE TO CAVITY STRUCTURE

In the cavity, acoustic waves travel between the reflectors, indicating that the magnon-phonon interaction length is effectively increased. Round-trip time due to the FP

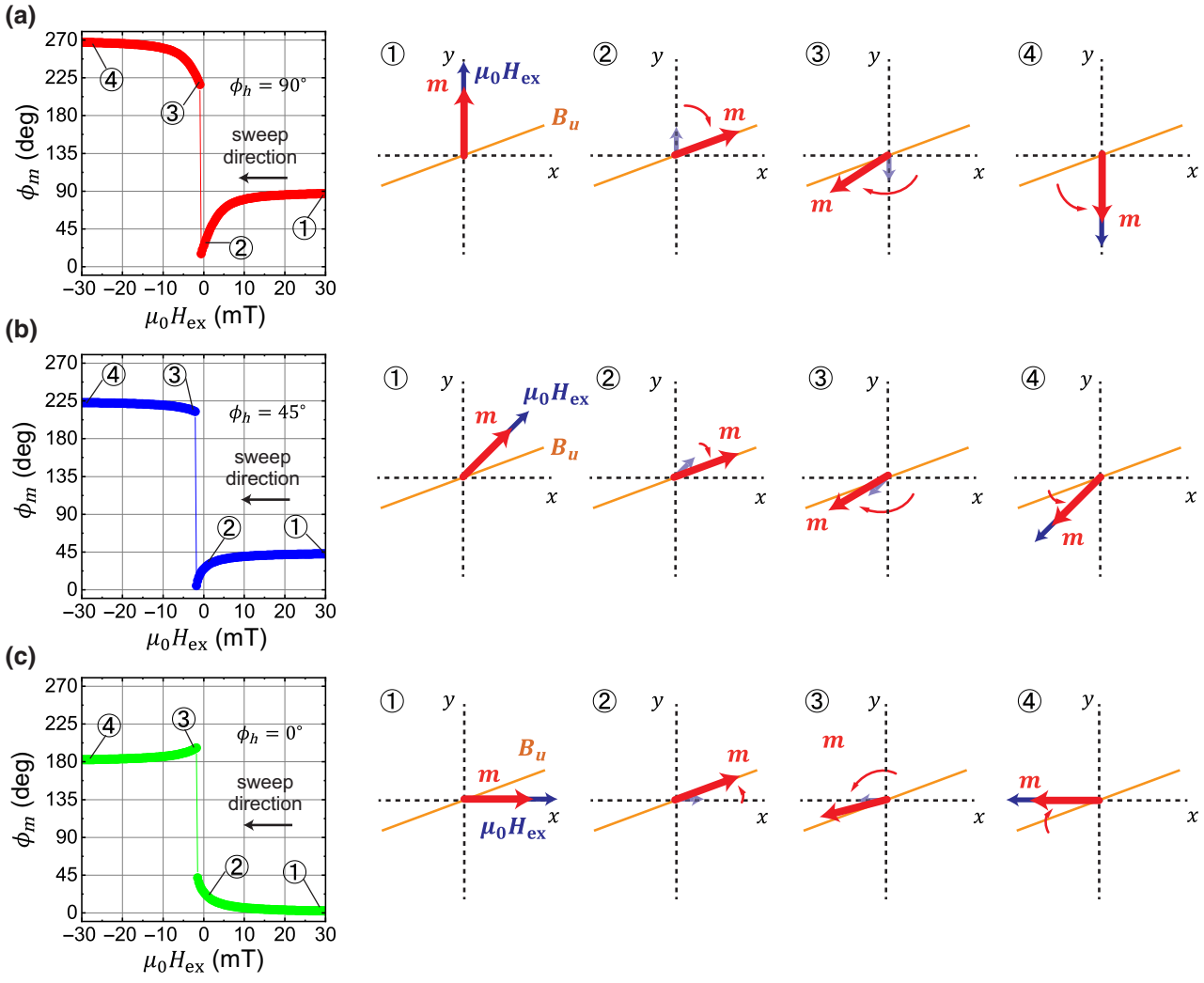

FIG. 8. Field dependence of magnetization angle ϕ_m at $\phi_h = 90°$ (a), $45°$ (b), and $0°$ (c). These calculations were performed in the backward field sweep condition. The right insets illustrate the magnetization orientation (red arrow, m) with respect to the field (blue arrow, $\mu_0 H_{\rm ex}$) and anisotropy field (yellow solid line, B_u) in the xy coordinate system at given fields labeled as ①, ②, ③, and ④ which are indicated in the left panels.

resonance is estimated by $N = v_{\mathrm{SAW}}\tau_a'/(2L_c) \approx 5.8$ with acoustic damping time τ_a' at $\mu_0 H_{\mathrm{ex}} = 1.2$ mT in $\phi_h = 90^\circ$ where the maximum absorption occurs as seen in Fig. 3(a). By normalizing the absorption power by the effective length $2Nw$, we obtain 7.1 dB/mm, which is comparable to the approximately $4 \sim 5$ dB/mm at 0.86 GHz in previous work [19,23,28].

APPENDIX F: MAGNETOSTRICTIVE EFFECT IN DIFFERENT FIELD SWEEP DIRECTIONS

Figure 9 shows the field dependence of normalized amplitude $|S_{21}|^2_{\mathrm{norm}}$ at $\phi_h = 45^\circ$ with forward and backward sweeps as denoted by gray and black solid lines. Acoustic absorption due to the spin-wave resonance excitation is observed at $\mu_0 H_{\mathrm{ex}} = \pm 2.1$ mT in both sweep directions, whereas an additional dip occurs in different fields as denoted by black arrows; $\mu_0 H_{\mathrm{ex}} = -1.5$ mT in the backward sweep and 1.5 mT in the forward one. This could be caused by the magnetization inversion process in the Ni film.

APPENDIX G: DESCRIPTION OF THE DYNAMICS VIA MAGNON-PHONON COUPLING

The dynamics of the acoustic mode interacting with the magnetization as macrospins via the magnetostrictive coupling is given by the following equation of motion:

$$\rho_a \ddot{U}_a(t) + \rho_a \kappa_a \dot{U}_a(t) + \rho_a \omega_a^2 U_a(t) - M_s b_{\mathrm{ma}} \sin 2\phi_m \frac{V_{\mathrm{a-m_2}}}{V_a} m_2(t) = F_d \tag{G1}$$

where U_a, κ_a, and ω_a are the displacement, damping rate, and angular frequency of the acoustic mode, and

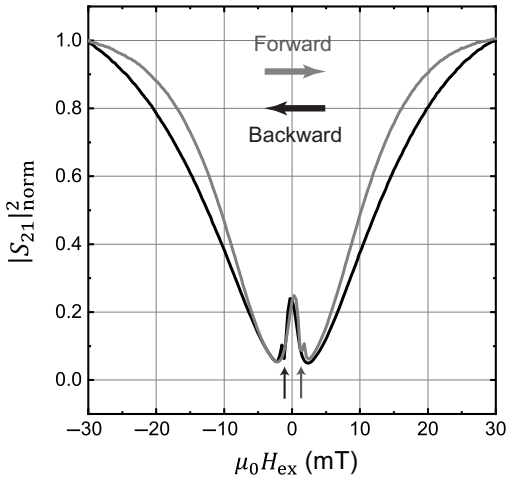

FIG. 9. Field dependence of SAW transmission magnitude $|S_{21}|^2_{\mathrm{norm}}$ excited at −10 dBm and in forward (gray) and backward (black) sweep directions. Sharp dips ascribed to the magnetization reversal are denoted by black arrows.

ρ_a is the density of the ferromagnet. The magnetostrictive coupling between the acoustic mode $U_a(t)$ and the magnetic precession component $m_2(t)$ [see Fig. 2(a)] is described in the fourth term on the left-hand side with the saturation magnetization M_s, magnetoelastic coupling constant b_{ma}, magnetization angle ϕ_m, mode volume of the acoustic mode $V_a \equiv \int dV[\Psi_a(\mathbf{r})]^2$, and the overlap integral $V_{\mathrm{a-m_2}} \equiv \int dV\left[\Psi_a(\mathbf{r})\partial_x \Psi_{m_2}(\mathbf{r})\right]$, with the spatial distribution of acoustic mode $\Psi_a(\mathbf{r})$ and that of macrospin $\Psi_{m_2}(\mathbf{r})$. The alternative coordinate system with (m_1, m_2, m_3) has transformation relation to the (m_x, m_y, m_z) coordinate system given by [19]

$$\begin{pmatrix} m_x \\ m_y \\ m_z \end{pmatrix} = \begin{pmatrix} 0 & -\sin\phi_m & \cos\phi_m \\ 0 & \cos\phi_m & \sin\phi_m \\ -1 & 0 & 0 \end{pmatrix} \begin{pmatrix} m_1 \\ m_2 \\ m_3 \end{pmatrix}. \tag{G2}$$

Note that each spatial distribution is normalized so that $\max_{\mathbf{r}}\left[\Psi_j(\mathbf{r})\right] = 1$. The driving force from the IDT electrodes is simply denoted by F_d.

On the other hand, the dynamics of macrospins $m_1(t)$ and $m_2(t)$ are given by the linearized Landau-Lifshitz-Gilbert (LLG) equations [19,28]

$$\frac{\alpha}{\gamma}\dot{m}_1(t) + (G_{11} - G_3)m_1(t) - \frac{1}{\gamma}\dot{m}_2(t) = 0, \tag{G3}$$

$$\frac{\alpha}{\gamma}\dot{m}_2(t) + (G_{22} - G_3)m_2(t) + \frac{1}{\gamma}\dot{m}_1(t) + b_{\mathrm{ma}} \sin 2\phi_m \frac{V_{\mathrm{m_2-a}}}{V_M} U_a(t) = 0. \tag{G4}$$

where α and γ are the Gilbert damping factor and gyromagnetic ratio of the Ni film, respectively. Each coefficient is given by $G_{11} = 2B_d$, $G_{22} = -2B_u \sin^2(\phi_m - \phi_u)$, and $G_3 = -\mu_0 H_{\mathrm{ex}} \cos(\phi_m - \phi_h) - 2B_u \cos^2(\phi_m - \phi_u)$, with the in-plane uniaxial anisotropy B_u and out-of-plane shape anisotropy B_d, along with the angle of the external magnetic field ϕ_h, that of the magnetization ϕ_m, and that of the uniaxial anisotropic field ϕ_u [see Fig. 2(a)]. The magnetostrictive coupling is given by the fourth term including the overlap integral $V_{\mathrm{m_2-a}} = \int dV[\Psi_m(\mathbf{r})\partial_x \Psi_a(\mathbf{r})]$ and the mode volume of the macrospin, $V_m \equiv \int dV[\Psi_{m_2}(\mathbf{r})]^2 = \int dV[\Psi_{m_1}(\mathbf{r})]^2$. Here we assume that the spatial distribution in the precession magnitude and phase of the macrospins is completely determined by that of strain, $\Psi_{m_1}(\mathbf{r}) \approx \Psi_{m_2}(\mathbf{r}) \approx \partial_x \Psi_a(\mathbf{r})$. The basic idea to derive the coupling term is found in elsewhere [19]. The LLG equations can be diagonalized to

$$\dot{m}_\pm(t) = \left(\pm i\omega_m - \frac{\kappa_m}{2}\right) m_\pm(t) \pm b_{\mathrm{ma}} \sin 2\phi_m \frac{V_{\mathrm{m_2-a}}}{V_m} \frac{\gamma}{1+\alpha^2} \eta U_a(t), \tag{G5}$$

where

$$\omega_m = \frac{\sqrt{4\tilde{G}_1\tilde{G}_2 - \alpha^2(\tilde{G}_1 - \tilde{G}_2)^2}}{2}, \tag{G6}$$

$$\kappa_m = \alpha(\tilde{G}_1 + \tilde{G}_2) \tag{G7}$$

and

$$\eta = -i\frac{\alpha}{2} - \frac{2\tilde{G}_1 + (\tilde{G}_1 - \tilde{G}_2)\alpha^2}{2\sqrt{4\tilde{G}_1\tilde{G}_2 - \alpha^2(\tilde{G}_1 - \tilde{G}_2)^2}} \tag{G8}$$

are defined with $\tilde{G}_j \equiv \gamma(G_{jj} - G_3)/(1+\alpha^2)$. Because $m_2 = i(m_+ + m_-)$, the equation of motion for the acoustic mode can be rewritten as

$$\rho_a\ddot{U}_a(t) + \rho_a\kappa_a\dot{U}_a(t) + \rho_a\omega_a^2 U_a(t) - iM_s b_{\rm ma}\sin 2\phi_m \frac{V_{\rm a-m_2}}{V_a}[m_+(t) + m_-(t)] = F_d. \tag{G9}$$

Because the acoustic mode is spatially distributed as a standing wave on the Ni film (i.e., $\Psi_a(\mathbf{r}) = \tilde{\Psi}_a(y,z)\sin kx$), we can simplify the spatial overlap as follows:

$$V_{\rm a-m_2} = -k\int dydz\int_{-w/2}^{w/2} dx\sin^2 kx = -\frac{kw}{2}\int dydz = -kV_{\rm ma}, \tag{G10}$$

$$V_{\rm m_2-a} = k\int dydz\int_{-w/2}^{w/2} dx\cos^2 kx = \frac{kw}{2}\int dydz = kV_{\rm ma}, \tag{G11}$$

where k is the wave vector of the acoustic mode and w is the width of Ni film along the propagation direction with the structural condition $w \gg k^{-1}$. By denoting $J \equiv kb_{\rm ma}\sin 2\phi_m V_{\rm ma}$, we achieve the simplified expression

$$\ddot{U}_a(t) + \kappa_a\dot{U}_a(t) + \omega_a^2 U_a(t) + i\frac{M_s J}{\rho_a V_a}[m_+(t) + m_-(t)] = F_d, \tag{G12}$$

$$\dot{m}_\pm(t) = \left(\pm i\omega_m - \frac{\kappa_m}{2}\right)m_\pm(t) \pm \frac{J}{V_m}\frac{\gamma}{1+\alpha^2}\eta U_a(t). \tag{G13}$$

Thus, by performing Fourier transformation on Eqs. (G12) and (G13), the displacement amplitude of acoustic waves (u_a) is given by

$$u_a(\omega) = \frac{F_d\rho_a^{-1}}{-(\omega^2 - \omega_a^2) - i\omega\kappa_a - J^2\chi_m(\omega)}, \tag{G14}$$

with the magnonic susceptibility

$$\chi_m(\omega) = \frac{2M_s\gamma\eta\omega_m}{\rho_a V_a V_m(1+\alpha^2)(-\omega^2 + \omega_m^2 + \frac{\kappa_m^2}{4} - i\kappa_m\omega)}. \tag{G15}$$

The normalized amplitude $|u_a|^2_{\rm norm}$ is comparable with $|S_{21}|^2_{\rm norm}$ because of the linear relation of u_a, ϵ_{xx} and a piezoelectric voltage (i.e., S_{21}). The representation of magnon-phonon coupling constant g is unveiled by performing the rotating frame approximation with transformations of $U_a(t) = \sqrt{(\hbar/2\omega_a\rho_a V_a)}A(t)e^{-i\omega_a t} + \text{c.c.}$ and $m_\pm(t) = \sqrt{[\hbar\gamma\eta/M_s V_m(1+\alpha^2)]}M_\pm(t)e^{\pm i\omega_m t}$ as follows:

$$\dot{A}(t) = -\frac{\kappa_a}{2}A(t) + gM_-(t) + \tilde{F}_d(t), \tag{G16}$$

$$\dot{M}_-(t) = -\frac{\kappa_m}{2}A(t) - gA(t), \tag{G17}$$

with

$$g = J\sqrt{\frac{M_s\gamma\eta}{2V_a V_m\rho_a(\omega_a + \frac{\kappa_m^2}{16\omega_a})(1+\alpha^2)}}. \tag{G18}$$

If $\omega_a \gg \kappa_m$, it can be simplified to

$$g \approx J\sqrt{\frac{M_s\gamma\eta}{2V_a V_m\omega_a\rho_a(1+\alpha^2)}} \tag{G19}$$

$$\approx kb_{\rm ma}\sin 2\phi_m\sqrt{\frac{M_s\gamma\eta}{2\omega_a\rho_a(1+\alpha^2)}}\frac{w}{L_c}\frac{d}{\lambda} \tag{G20}$$

where $\tilde{F}_d$ is the resonance driving force in the rotating frame, L_c is the acoustic cavity length along the propagation direction, d is the Ni film thickness, and λ is the wavelength of the acoustic mode approximated to be the penetration depth of the acoustic mode in the Ni film. Note that the final approximation in Eq. (G20) is obtained by assuming that $\Psi_a(\mathbf{r}) \approx D_0 e^{-z/\lambda}\sin kx$ with an arbitrary constant D_0. Here, we emphasize that $A(t)$ and $M(t)$ have no dimension unit, which implies that the quantization of each amplitude brings them to the description for quantum dynamics as well as the formulation given in magnon-phonon hybrid quantum systems [38–40].

APPENDIX H: ACOUSTIC AND MAGNETIC PARAMETERS FOR SIMULATIONS

All the parameters used in the simulations are shown in the table below, and they are in good agreement with previous reports [19,28]. Only the value of ϕ_u is chosen in such a way that this gives the best reproduction of the experimental data with Eq. (3).

b_{ma}	Magnetoelastic coupling constant	14 T
B_d	Out-of-plane shape anisotropy	0.21 T
B_u	In-plane uniaxial anisotropy	1.8 mT
ϕ_u	Angle of in-plane uniaxial anisotropy	25°
α	Gilbert damping factor	0.08
M_s	Saturation magnetization	370 kA/m
γ	Gyromagnetic ratio	$2.185\mu_B/\hbar$
ρ_a	Mass density	8900 kg/m^3

APPENDIX I: FIELD DEPENDENCE OF SPIN-WAVE RESONANCE FREQUENCY AND DAMPING RATE

Figure 10 shows the backward field sweep response of spin-wave resonance frequency (ω_m) and damping rate (κ_m) calculated by Eqs. (G6) and (G7) at $\phi_h = 90°$ (red), 45° (blue), and 0° (green). The resonance frequency of the acoustic cavity $\omega_a/2\pi = 0.975$ GHz is denoted by a black solid horizontal line in the top panel. As the field is reduced from $\mu_0 H_{ex} = 30$ mT, ω_m decreases and gradually approaches ω_a. Perfect frequency matching $\omega_m = \omega_a$ is realized at $\mu_0 H_{ex} = -0.6$ mT for all three ϕ_hs. However, this configuration is fragile and susceptible to tiny fluctuations in $\mu_0 H_{ex}$ at $\phi_h = 45°$ and 0°. In contrast, ω_m can keep the frequency nearly constant and close to ω_a between $\mu_0 H_{ex} = 4$ mT and -4 mT at $\phi_h = 90°$, where $\omega_m \approx \omega_a$ is fulfilled because of $|\omega_m - \omega_a| < \kappa_m/2$ as shown in the bottom panel. Moreover, at this field angle, $\phi_m = 45°$ is achieved around $\mu_0 H_{ex} = 1.2$ mT so that the maximum magnetostriction factor J is available [see Eq. (2) in the main text].

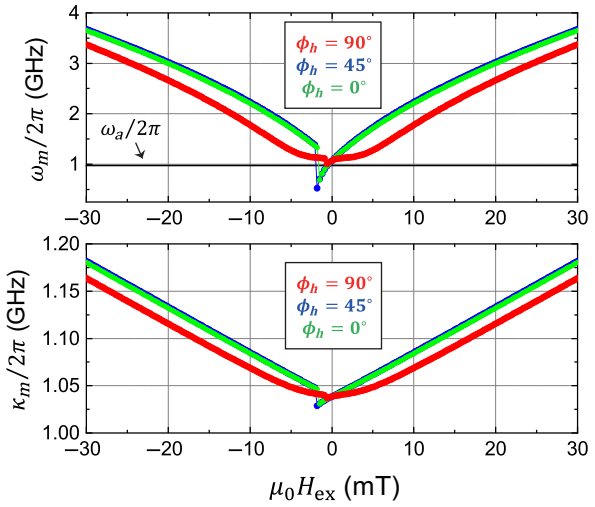

FIG. 10. Field dependence of spin-wave resonance frequency $\omega_m/2\pi$ (top) and magnetic damping $\kappa_m/2\pi$ (bottom) at $\phi_h = 90°$ (red), 45° (blue), and 0° (green). These calculations were performed in the backward field sweep condition. The resonance frequency of the acoustic cavity $\omega_a/2\pi$ is denoted by a black solid line in the top panel.

[1] M. Aspelmeyer, T. J. Kippenberg, and F. Marquardt, Cavity optomechanics, Rev. Mod. Phys. **86**, 1391 (2014).

[2] J. Chan, T. P. M. Alegre, A. H. Safavi-Naeini, J. T. Hill, A. Krause, S. Gröblacher, M. Aspelmeyer, and O. Painter, Laser cooling of a nanomechanical oscillator into its quantum ground state, Nature **478**, 89 (2011).

[3] P. F. Cohadon, A. Heidmann, and M. Pinard, Cooling of a Mirror by Radiation Pressure, Phys. Rev. Lett. **83**, 3174 (1999).

[4] T. J. Kippenberg and K. J. Vahala, Cavity optomechanics back-action at the mesoscale, Science **321**, 1172 (2008).

[5] A. D. O'Connell, M. Hofheinz, M. Ansmann, R. C. Bialczak, M. Lenander, E. Lucero, M. Neeley, D. Sank, H. Wang, and M. Weides *et al.*, Quantum ground state and single-phonon control of a mechanical resonator, Nature **464**, 697 (2010).

[6] J. D. Teufel, T. Donner, D. Li, J. W. Harlow, M. S. Allman, K. Cicak, A. J. Sirois, J. D. Whittaker, K. W. Lehnert, and R. W. Simmonds, Sideband cooling micromechanical motion to the quantum ground state, Nature **475**, 359 (2011).

[7] P. Arrangoiz-Arriola, E. A. Wollack, Z. Wang, M. Pechal, W. Jiang, T. P. McKenna, J. D. Witmer, R. V. Laer, and A. H. Safavi-Naeini, Resolving the energy levels of a nanomechanical oscillator, Nature **571**, 537 (2019).

[8] Y. Chu, P. Kharel, W. H. Renninger, L. D. Burkhart, L. Frunzio, P. T. Rakich, and R. J. Schoelkopf, Quantum acoustics with superconducting qubits, Science **358**, 199 (2017).

[9] M. V. Gustafsson, T. Aref, A. F. Kockum, M. K. Ekström, G. Johansson, and P. Delsing, Propagating phonons coupled to an artificial atom, Science **346**, 207 (2014).

[10] M. V. Gustafsson, P. V. Santos, G. Johansson, and P. Delsing, Local probing of propagating acoustic waves in a gigahertz echo chamber, Nat. Phys. **8**, 338 (2012).

[11] R. Manenti, A. F. Kockum, A. Patterson, T. Behrle, J. Rahamin, G. Tancredi, F. Nori, and P. J. Leek, Circuit quantum acoustodynamics with surface acoustic waves, Nat. Commun. **8**, 975 (2017).

[12] A. Noguchi, R. Yamazaki, Y. Tabuchi, and Y. Nakamura, Qubit-Assisted Transduction for a Detection of Surface Acoustic Waves near the Quantum Limit, Phys. Rev. Lett. **119**, 180505 (2017).

[13] Ö. O. Soykal, R. Ruskov, and C. Tahan, Sound-Based Analogue of Cavity Quantum Electrodynamics in Silicon, Phys. Rev. Lett. **107**, 235502 (2011).

[14] K. J. Satzinger, Y. P. Zhong, H.-S. Chang, G. A. Peairs, A. Bienfait, M.-H. Chou, A. Y. Cleland, C. R. Conner, É. Dumur, and J. Grebel *et al.*, Qunatum control of surface acoustic-wave phonons, Nature **563**, 661 (2018).

[15] M. J. A. Schuetz, E. M. Kessler, G. Giedke, L. M. K. Vandersypen, M. D. Lukin, and J. I. Cirac, Universal Quantum Transducers Based on Surface Acoustic Waves, Phys. Rev. X **5**, 031031 (2015).

[16] C. A. Potts, E. Varga, V. A. Bittencourt, S. V. Kusminskiy, and J. P. Davis, Dynamical Backaction Magnomechanics, Phys. Rev. X **11**, 031053 (2021).

[17] X. Zhang, C.-L. Zou, L. Jiang, and H. X. Tang, Cavity magnomechanics, Sci. Adv. **2**, e1501286 (2016).

[18] K. An, A. N. Litvinenko, R. Kohno, A. A. Fuad, V. V. Naletov, L. Vila, U. Ebels, G. de Loubens, H. Hurdequint, and N. Beaulieu *et al.*, Coherent long-range transfer of angular momentum between magnon kittel modes by phonons, Phys. Rev. B **101**, 060407(R) (2020).

[19] L. Dreher, M. Weiler, M. Pernpeintner, H. Huebl, R. Gross, M. S. Brandt, and S. T. B. Goennenwein, Surface acoustic wave driven ferromagnetic resonance in nickel thin films: Theory and experiment, Phys. Rev. B **86**, 134415 (2012).

[20] A. Hernández-Mínguez, F. Macià, J. M. Hernàndez, J. Herfort, and P. V. Santos, Large Nonreciprocal Propagation of Surface Acoustic Waves in Epitaxial Ferromagnetic/semiconductor Hybrid Structures, Phys. Rev. Appl. **13**, 044018 (2020).

[21] T. Kikkawa, K. Shen, B. Flebus, R. A. Duine, K.-I. Uchida, Z. Qiu, G. E. Bauer, and E. Saitoh, Magnon Polarons in the Spin Seebeck Effect, Phys. Rev. Lett. **117**, 207203 (2016).

[22] D. Kobayashi, T. Yoshikawa, M. Matsuo, R. Iguchi, S. Maekawa, E. Saitoh, and Y. Nozaki, Spin Current Generation Using a Surface Acoustic Wave Generated via Spin-Rotation Coupling, Phys. Rev. Lett. **119**, 077202 (2017).

[23] D. Labanowski, V. P. Bhallamudi, Q. Guo, C. M. Purser, B. A. McCullian, P. C. Hammel, and S. Salahuddin, Voltage-driven, local, and dfficient excitation of nitrogen-vacancy centers in diamond, Sci. Adv. **4**, eaat6574 (2018).

[24] R. Sasaki, Y. Nii, and Y. Onose, Surface acoustic wave coupled to magnetic resonance on multiferroic CuB_2O_4, Phys. Rev. B **99**, 014418 (2019).

[25] R. Sasaki, Y. Nii, and Y. Onose, Magnetization control by angular momentum transfer from surface acoustic wave to ferromagnetic spin moments, Nat. Commun. **12**, 1 (2021).

[26] P. J. Shah, D. A. Bas, I. Lisenkov, A. Matyushov, N. X. Sun, and M. R. Page, Giant nonreciprocity of surface acoustic waves enabled by the magnetoelastic interaction, Sci. Adv. **6**, eabc5648 (2020).

[27] L. Thevenard, C. Gourdon, J. Y. Prieur, H. J. von Bardeleben, S. Vincent, L. Becerra, L. Largeau, and J.-Y. Duquesne, Surface-acoustic-wave-driven ferromagnetic resonance in (Ga, Mn)(As, P) epilayers, Phys. Rev. B **90**, 094401 (2014).

[28] M. Weiler, L. Dreher, C. Heeg, H. Huebl, R. Gross, M. S. Brandt, and S. T. B. Goennenwein, Elastically Driven Ferromagnetic Resonance in Nickel Thin Films, Phys. Rev. Lett. **106**, 117601 (2011).

[29] M. Xu, K. Yamamoto, J. Puebla, K. Baumgaertl, B. Rana, K. Miura, H. Takahashi, D. Grundler, S. Maekawa, and Y. Otani, Nonreciprocal surface acoustic wave propagation via magneto-rotation coupling, Science Adv. **6**, eabb1724 (2020).

[30] D. D. Awschalom, C. Du, R. He, J. Heremans, A. Hoffmann, J. Hou, H. Kurebayashi, Y. Li, L. Liu, and V. Novosad *et al.*, Quantum engineering with hybrid magnonics systems and materials, IEEE Transactions on Quantum Engineering (2021).

[31] Y. Li, C. Zhao, W. Zhang, A. Hoffmann, and V. Novosad, Advances in coherent coupling between magnons and acoustic phonons, APL Mater. **9**, 060902 (2021).

[32] T. Kawada, M. Kawaguchi, T. Funato, H. Kohno, and M. Hayashi, Acoustic spin hall effect in strong spin-orbit metals, Sci. Adv. **7**, eabd9697 (2021).

[33] L. Shao, S. Maity, L. Zheng, L. Wu, A. Shams-Ansari, Y.-I. Sohn, E. Puma, M. N. Gadalla, M. Zhang, and C. Wang *et al.*, Phononic Band Structure Engineering for High-Q Gigahertz Surface Acoustic Wave Resonators on Lithium Niobate, Phys. Rev. Appl. **12**, 014022 (2019).

[34] Y. Xu, W. Fu, C. ling Zou, Z. Shen, and H. X. Tang, High quality factor surface fabry-perot cavity of acoustic waves, Appl. Phys. Lett. **112**, 073505 (2018).

[35] K. Yamada, H. Takemura, Y. Inoue, T. Omi, and S. Matsumura, Effect of Li/Nb ratio on the saw velocity of 128°Y-X $LiNbO_3$ wafers, Jpn. J. Appl. Phys. **26**, 219 (1987).

[36] D. Hatanaka and H. Yamaguchi, Real-Space Characterization of Cavity-Coupled Waveguide Systems in Hypersonic Phononic Crystals, Phys. Rev. Appl. **13**, 024005 (2020).

[37] M. Hamoumi, P. E. Allain, W. Hease, E. Gil-Santos, L. Morgenroth, B. Gérard, A. Lemaître, G. Leo, and I. Favero, Microscopic Nanomechanical Dissipation in Gallium Arsenide Resonators, Phys. Rev. Lett. **120**, 223601 (2018).

[38] J. Li and S.-Y. Zhu, Entangling two magnon modes via magnetostrictive interaction, New J. Phys. **21**, 085001 (2019).

[39] J. Li, S.-Y. Zhu, and G. S. Agarwal, Magnon-Photon Entanglement in Cavity Magnomechanics, Phys. Rev. Lett. **121**, 203601 (2018).

[40] H. Tan and J. Li, Einstein-Podolsky-Rosen entanglement and asymmetric steering between distant magcroscopic mechanical and magnonic systems, Phys. Rev. Res. **3**, 013192 (2021).